Journal of Materials Chemistry C

Role of Annealing Atmosphere on the Crystal Structure and Composition of Tetrahedrite-Tennantite Alloy Nanoparticles

Journal:	*Journal of Materials Chemistry C*
Manuscript ID	TC-ART-06-2018-002762.R1
Article Type:	Paper
Date Submitted by the Author:	30-Aug-2018
Complete List of Authors:	McClary, Scott; Purdue University, Davidson School of Chemical Engineering Balow, Robert; Purdue University, Department of Chemistry Agrawal, Rakesh; Purdue University, Davidson School of Chemical Engineering

Role of Annealing Atmosphere on the Crystal Structure and Composition of Tetrahedrite-Tennantite Alloy Nanoparticles

Scott A. McClary*†, Robert B. Balow**†, and Rakesh Agrawal*

*Davidson School of Chemical Engineering, Purdue University, 480 Stadium Mall Drive, West Lafayette, IN 47907.

**Department of Chemistry, Purdue University, 560 Oval Drive, West Lafayette, IN 47907.

†Denotes equal contribution to the manuscript.

Abstract

Tetrahedrite-tennantite (TET-TEN, $Cu_{12}Sb_4S_{13}$-$Cu_{12}As_4S_{13}$) nanoparticle (NP) alloys spanning the entire Sb-As composition range were synthesized using a hot-injection method without any detectable impurities. Thin films of TET-TEN NPs were prepared from colloidal NP inks and heat treated in sulfur vapor, hydrogen sulfide, and nitrogen atmospheres. Under sulfur, the TET-TEN films were oxidized to tetragonal famatinite-luzonite ($Cu_3As_{1-x}Sb_xS_4$). Heat treating under a reducing hydrogen sulfide atmosphere stabilized the mixed TET-TEN alloy compositions, though the endmember compositions partially decomposed via loss of volatile pnictogen sulfides. Losses of pnictogen and sulfur atoms were most significant when heat treating under an inert nitrogen atmosphere. Collectively, these results suggest that TET-TEN materials can be reversibly interconverted to famatinite-luzonite by selecting an appropriate annealing atmosphere. Our work serves as the foundation for both the synthesis and production of device-quality TET-TEN and related chalcogenide NP thin films.

1. Introduction

Semiconducting nanoparticles (NPs) offer many advantages over bulk materials for the fabrication of thin-film electronic devices due to their size-dependent characteristics.

Optoelectronic properties of NPs are correlated with NP size due to quantum confinement effects, and NP surfaces can be functionalized with a variety of ligands for colloidal stability in many solvents, thus enabling the use of low-cost and high-throughput manufacturing methods such as direct inkjet printing.[1–3] These qualities have spurred significant scientific effort into synthesizing novel NP-based semiconducting compounds for use in energy-related applications. High-efficiency photovoltaic devices have been demonstrated for NP-based CdTe[4,5] and $Cu(In,Ga)Se_2$,[6] and a high figure of merit has been reported for NP-based Bi_2Te_3 thermoelectric devices.[7]

While long-chained carbonaceous ligands enable facile solution-phase deposition of NP films, they typically hinder final device performance due to their electrically insulating nature. As such, as-deposited NP thin films are often heat treated to remove or modify the surface-bound ligands and improve electronic transport. For sulfide-based materials, a variety of thermal anneals have been incorporated into thin film fabrication protocols. Elemental sulfur and hydrogen sulfide (H_2S) have both been used to remove ligands and densify NP films of Cu_2ZnSnS_4 and $Cu(In,Ga)S_2$, respectively.[8,9] The use of a reactive selenium atmosphere to convert $CuInS_2$ and $CuInSe_2$ NP films into micron-sized grains of $CuInSe_2$ was first demonstrated by Guo et al.[10,11] This heat treatment is now a widely-used method to convert sulfide-based materials into their selenide analogs and aggregate carbonaceous ligands into a "fine-grain" layer whose effect on device performance appears to be relatively benign.[12–15]

Recent energy-related research has seen an increased focus on semiconductors comprised of earth-abundant elements to minimize feedstock expenses and alleviate concerns regarding large-scale materials availability for terawatt-scale manufacturing.[16] One such class of materials is the copper antimony sulfide (Cu-Sb-S) family, which has been studied in both thermoelectric and

photovoltaic contexts. Extensive research on tetrahedrite (TET, $Cu_{12}Sb_4S_{13}$), has revealed promising thermoelectric properties in natural, synthetic, and alloyed samples.[17–25] Additionally, TET and its derivatives are candidates for use in solar energy conversion due to predicted conversion efficiencies exceeding 20% and ideal band gap energies of ~1.5 eV.[26,27]

The isostructural analog of TET, achieved by substituting antimony with the more earth abundant element arsenic, is tennantite (TEN, $Cu_{12}As_4S_{13}$).[28–30] The TET-TEN system forms a complete solid series between Sb and As, enabling the tuning of optoelectronic properties via alloying.[31,32] Furthermore, the mismatch of Sb and As radii in a mixed alloy crystal lattice may improve thermoelectric performance by increasing phonon scattering without significantly hindering carrier transport.[33] Sb-As alloying has been shown to tune the optical band gap in $Cu_3As_{1-x}Sb_xS_4$ NPs,[30] improve the power factor (a thermoelectric parameter) of $Cu_3As_{1-x}Sb_xSe_4$ NP films,[34] and boost the thermoelectric figure of merit in blended TET-TEN mineral samples.[17,18]

Controlled syntheses of TET[35–38] and TEN[39] NPs have been previously reported in the literature. Development of a solution-based synthesis represents a more scalable route to Sb- and As-based chalcogenide films when compared to more common techniques such as spark plasma sintering. Developing thermal treatments to remove surface-bound ligands and densify NP-based TET-TEN films is necessary for future optoelectronic device development; however, there have been no reports detailing a synthetic protocol for TET-TEN NP alloys or heat treatments for thin films formed from such NPs. In this manuscript, we report the first synthesis of impurity-free TET-TEN NP alloys and demonstrate the effects of elemental sulfur, H_2S, and inert atmospheres on the phase stability and composition of TET-TEN NP alloy films at elevated temperatures. We show that the oxidation state of sulfur during heat treatment is critical for controlling the final

bulk phase of the film, and that arsenic, antimony, and sulfur are prone to escaping from the films at elevated temperatures. These data are critical knowledge for future development of Cu-Sb-S, Cu-As-S, and related material systems.

2. Experimental Section

Materials

All materials were used as received with standard air-free handling procedures. Antimony (III) chloride ($SbCl_3$, 99.99%), arsenic (III) chloride ($AsCl_3$, 99.95%), and sulfur flakes (S, 99.99%) were obtained from Sigma-Aldrich. Copper (I) chloride (CuCl, 99.99%) was obtained from Strem. Oleylamine (80-90%, OLA) was obtained from Acros Organics; it was degassed by three freeze-pump-thaw (FPT) cycles and stored in a nitrogen-filled glovebox before use in making stock solutions. Ethanol (EtOH, 200 proof) was obtained from Koptec, hexanes (98.5%, mixture of isomers) were obtained from Fisher, and toluene (99.5%) was obtained from Macron. Hydrogen sulfide (H_2S, 1%; balance argon) was obtained from Airgas (an Air Liquide Company). *Note that $AsCl_3$ is highly toxic and must be handled under an inert atmosphere using proper personal protective equipment at all times!*

Nanoparticle Alloy Synthesis and Washing Procedure

To synthesize TET-TEN NP alloys, a two-step hot injection method was adapted from previous reports by Balow et al.[30,39] All syntheses were performed using standard air-free techniques. Three stock solutions were prepared in a nitrogen-filled glovebox. Solution A contained 1.6 mmol CuCl, 0.571 mmol $SbCl_3$, and 8 mL FPT OLA; Solution B contained 1.6 mmol CuCl, 0.571 mmol $AsCl_3$, and 8 mL FPT OLA; Solution C contained 9 mmol S flakes and 6 mL FPT OLA. All solutions were sealed and placed on a stir plate and heated to 65 °C for dissolution. Solutions A and B stirred with heat for 2 h, while Solution C stirred for 0.5 h with

heat and the remaining 1.5 h without heat. Immediately prior to injection, mixed cation precursor solutions were made by combining Solutions A and B in nitrogen-purged vials sealed with Teflon septa. The $Cu_{12}Sb_4S_{13}$ precursor solution contained 3.0 mL of Solution A, the $Cu_{12}(As_{0.25}Sb_{0.75})_4S_{13}$ solution contained 2.25 mL of Solution A and 0.75 mL of Solution B, the $Cu_{12}(As_{0.50}Sb_{0.50})_4S_{13}$ solution contained 1.5 mL of Solution A and 1.5 mL of Solution B, the $Cu_{12}(As_{0.75}Sb_{0.25})_4S_{13}$ solution contained 0.75 mL of Solution A and 2.25 mL of Solution B, and the $Cu_{12}As_4S_{13}$ solution contained 3.0 mL of Solution B.

A three-neck reaction flask containing 7.0 mL OLA and a Teflon stir bar was sealed and attached to a Schlenk line. The flask was evacuated and refilled three times with argon. The flask was then heated under vacuum to reflux (~115 °C) for 1 h. The flask was then refilled with argon, and the temperature was increased to 250 °C. Once the temperature reached 250 °C, 0.8 mL of S-OLA (Solution C) was injected into the vessel, and 2.0 mL of the appropriate mixed cation solution was injected 20 s later, inducing a rapid nucleation event. The reaction was maintained at 250 °C for 30 min and then cooled naturally to room temperature. Once the vessel was below 40 °C, the flask contents were extracted into a 25 mL centrifuge tube for washing and purification. The centrifuge tube was topped with EtOH and centrifuged at 14,000 rpm (~17100 xG) for 5 min. The supernatant was discarded, and the pellet was resuspended in ~10 mL hexane by vortexing. The tube was then topped with EtOH, vortexed, and centrifuged as described previously. The hexane-ethanol wash was repeated one final time. The remaining NP pellet was suspended in ~5 mL toluene and stored for later use.

Heat Treatments

Samples were prepared for heat treatments by drop-casting ~200 μL of the toluene NP ink onto glass and silicon substrates. The toluene was then slowly evaporated at room

temperature in air to form thin films. For each heat treatment, the five samples of distinct compositions were treated together in the same vessel.

Sulfur Anneal

The sulfur anneals occurred in a three-zone tube furnace (Applied Test Systems, Inc. Series 3210) with a quartz tube. Zone 1 contained sulfur flakes, Zone 2 contained the samples, and Zone 3 was left empty. The tube was evacuated and refilled with argon three times to purge the system of oxygen and moisture. Zone 1 was heated to 200 °C, and the other two zones were heated to the desired reaction temperature (350 °C or 450 °C). A steady backflow of argon (10 sccm) was introduced to minimize sulfur transport towards the samples during the initial heat up. Once the temperatures had equilibrated, a graphite box containing sulfur flakes was pushed into Zone 1 to heat the sulfur flakes and generate sulfur vapor (15 min). Then, the five thin films were inserted into Zone 2 using a manual push-pull rod, and the argon flow was reversed to carry sulfur vapor towards the samples for 1 h. After the sulfurization, the furnace was opened, and the heaters were turned off. The direction of the argon flow was again reversed to purge the atmosphere and minimize condensation of sulfur onto the thin films. The samples were naturally cooled below 40 °C before removing the samples to ambient air.

Hydrogen Sulfide (H_2S) Anneal

The five samples were loaded into a graphite sample holder and secured outside the heating zone of a vertical tube furnace (Applied Test Systems, Inc., Series 3210). A quartz tube was placed over the samples and sealed within the furnace. The H_2S and argon gas lines were purged with argon for 10 min. The tube was then evacuated and refilled with argon three times and then heated to the annealing temperature (350 °C or 450 °C) under 100 sccm argon flow. Once the target temperature was reached, the argon lines were closed, and H_2S/Ar gas flow was

initiated (20 sccm). After 1 min, the samples were pushed into the center of the tube furnace using a manual push-pull rod and treated for 1 h. The heaters were then turned off, the H_2S/Ar flow was halted, and a 100 sccm argon flow was initiated. The furnace jacket was opened, allowing the samples to cool naturally to 40 °C before opening the tube to ambient air.

Hydrogen sulfide is highly toxic and corrosive. To ensure safe operation, both the hydrogen sulfide tank and annealing furnace are stored within a fume hood. The furnace is equipped with an H_2S detector with a solenoid shutoff valve that will close in the event of a detectable leak above 10 ppm. The concentration of H_2S is 1%, which is below the lower flammability limit (LFL) of 4%; more stringent safety precautions must be taken when working at higher concentrations. The gas outlet of the furnace is also equipped with an aqueous 0.5 M copper (II) sulfate solution to scrub any residual H_2S gas from the exhaust.

Nitrogen Anneal

The five samples were placed on a ceramic hot plate and isolated from the ambient atmosphere using a custom-made bell jar that was sealed to the hot plate with vacuum grease. The top of the bell jar was connected to a vacuum and nitrogen purge line. The apparatus was evacuated and refilled with nitrogen three times. The inlet nitrogen flow was set to 7 cfm using a rotameter, and the vacuum pump was adjusted such that the internal pressure of the bell jar was maintained at 100 torr. The hot plate was set to the desired temperature (350 °C or 450 °C) for 1 h. After the treatment, the samples were cooled naturally to 40 °C before returning to atmospheric pressure and opening to the ambient environment.

Characterization

Grazing incidence X-ray diffraction (GIXRD) data were collected on a Rigaku Smartlab diffractometer equipped with a copper Kα x-ray source. Parallel beam geometry was used with

an incidence angle of 0.5°. Raman spectra were collected using a Horiba/Jobin-Yvon LabRAM HR800 confocal microscope equipped with a 633 nm He:Ne laser through a 100x objective lens. Scanning electron microscopy (SEM) images were taken using either an FEI Nova NanoSEM at an accelerating voltage of 5 kV or a FEI Quanta 3D FEG dual-beam field emission SEM at an accelerating voltage of 7 kV. Scanning electron microscopy energy dispersive X-ray spectroscopy data (SEM-EDS) were collected using a FEI Quanta 3D FEG dual-beam field emission SEM at an accelerating voltage of 20 kV with an Oxford INCA Xstream-2 silicon drift detector. All SEM-EDS was analyzed using AZtec software. Rietveld refinement was conducted using MAUD software.

3. Results and Discussion

Characterization of Synthesized $Cu_{12}(As_{1-x}Sb_x)_4S_{13}$ Nanoparticles

The as-synthesized alloy NPs have a cubic crystal structure (space group I-43m) as determined using GIXRD (Fig. 1). All observed diffraction peaks in the endmember TET and TEN compositions are assignable to references for $Cu_{12}Sb_4S_{13}$ (JCPDS 01-075-2211) and $Cu_{12}As_4S_{13}$ (JCPDS 01-073-3934), respectively. The most intense reflections are indexed to the (222), (440), and (622) planes for both cubic TET and TEN. The cubic alloy series displays a linear shift in lattice parameter, as predicted by Vegard's Law for alloy materials (ESI†; Figure S1).[40,41] No extraneous diffraction planes are observed in the GIXRD patterns, suggesting an impurity-free synthesis.

Raman spectra of the $Cu_{12}(As_{1-x}Sb_x)_4S_{13}$ NPs were collected to check for amorphous impurity phases (Fig. 1). The TET and TEN endmember compositions closely match reference spectra for mineral $Cu_{12}Sb_4S_{13}$ (RRUFF ID R040164) and $Cu_{12}As_4S_{13}$ (RRUFF ID R050474), respectively, with slight discrepancies resulting from heavier elemental impurities (e.g. Zn, Ag)

in the reference spectra. All mixed compositions exhibit lattice vibrational modes (100 – 150 cm^{-1}) and symmetric (Sb/As)-S stretching modes (350 – 390 cm^{-1}) similar to those found in the endmember reference spectra. The peaks display two-mode behavior, and the position of each peak shifts slightly with changing composition; both observations are consistent with a previous report.[42] Only the vibrational modes reported for TET and TEN spectra were detected, further indicating impurity-free NPs.

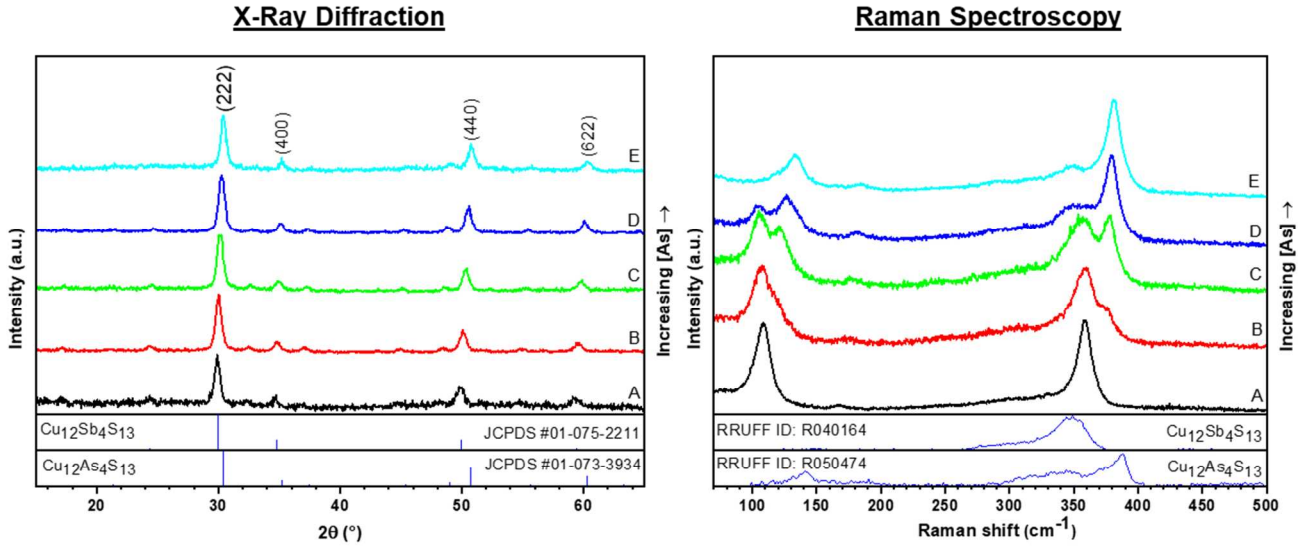

Figure 1. Grazing incidence X-ray diffraction (GIXRD) and Raman spectra of as-synthesized (A) $Cu_{12}Sb_4S_{13}$, (B) $Cu_{12}(As_{0.25}Sb_{0.75})_4S_{13}$, (C) $Cu_{12}(As_{0.50}Sb_{0.50})_4S_{13}$, (D) $Cu_{12}(As_{0.75}Sb_{0.25})_4S_{13}$, and (E) $Cu_{12}As_4S_{13}$ NPs. No secondary peaks were detected, suggesting the formation of impurity-free NPs.

The bulk elemental composition of the nano-sized particles (ESI†, Figure S2) was investigated by SEM-EDS (Table 1); the results suggest off-stoichiometric compositions. Such off-stoichiometry is not surprising, as NP surfaces are commonly cation-rich due to preferential binding of electron-donating ligands to under-coordinated metallic surface sites.[43] Furthermore,

variable composition ranges (particularly copper-rich compositions) in both the TET and TEN systems have been reported previously.[28,29,44–47]

Table 1. Calculated elemental ratios of as-synthesized $Cu_{12}(As_{1-x}Sb_x)_4S_{13}$ NPs from SEM-EDS data. The standard deviations are based on three measurements from random areas of each sample. Note that the stoichiometric ratios for Cu/(Sb+As) and (Cu+Sb+As)/S are 3.00 and 1.23, respectively.

$\boldsymbol{Target\ Composition}$	$\boldsymbol{\frac{Cu}{Sb+As}}$	$\boldsymbol{\frac{Sb}{Sb+As}}$	$\boldsymbol{\frac{Cu+Sb+As}{S}}$
$Cu_{12}Sb_4S_{13}$	2.86 ± 0.05	1.00 ± 0.00	1.32 ± 0.02
$Cu_{12}(As_{0.25}Sb_{0.75})_4S_{13}$	3.09 ± 0.05	0.76 ± 0.00	1.39 ± 0.01
$Cu_{12}(As_{0.50}Sb_{0.50})_4S_{13}$	3.28 ± 0.07	0.55 ± 0.00	1.40 ± 0.04
$Cu_{12}(As_{0.75}Sb_{0.25})_4S_{13}$	3.45 ± 0.21	0.28 ± 0.01	1.45 ± 0.06
$Cu_{12}As_4S_{13}$	3.10 ± 0.02	0.00 ± 0.00	1.35 ± 0.01

Characterization of Nanoparticles Annealed in Sulfur

GIXRD data (Fig. 2) indicate complete conversion from the cubic TET-TEN alloy series to structures containing fully oxidized arsenic and antimony with a nominal stoichiometry of $Cu_3As_{1-x}Sb_xS_4$. These alloys have a tetragonal crystal structure corresponding to the famatinite-luzonite (FAM-LUZ, Cu_3SbS_4-Cu_3AsS_4) mineral series. The diffraction patterns of the purely Sb and As samples match with the respective FAM and LUZ references (JCPDS 01-071-0555 and JCPDS 01-074-1125); we attribute a slight difference in peak position between the Cu_3AsS_4 reference and heat treated sample to the presence of antimony in reference spectrum JCPDS 01-074-1125. A shift to higher 2θ was observed as the ratio of arsenic to antimony increased, suggesting a contraction of the unit cell as arsenic occupies antimony sites in the lattice. Arsenic-

rich compositions show an additional, but minor reflection around 28° 2θ that is assignable to the (210) plane of the orthorhombic polymorph enargite (ENG, Cu_3AsS_4, JCPDS 01-082-1464). Additionally, the intensity of this peak is reduced with increasing antimony concentration, suggesting that the tetragonal crystal structure is stabilized by the incorporation of antimony in the lattice. Rietveld refinement (ESI†, Table S1) confirms that increasing the antimony concentration decreases the relative proportion of the orthorhombic phase in the final film. The preferential formation of the tetragonal phase at high Sb concentrations is expected, as the FAM-LUZ series freely substitutes Sb and As at pnictogen lattice sites, while the ENG phase only remains stable up to ~12 at. % Sb substitution at As sites.[29,48]

Raman spectroscopy data (Fig. 2) also indicate the conversion of TET-TEN NP films to the FAM-LUZ alloy series upon heat treatment in a sulfur atmosphere at 450 °C. The vibrational modes of the Sb endmember match well with the Cu_3SbS_4 reference mineral (RRUFF ID R110021), while the As endmember is slightly shifted from the Cu_3AsS_4 reference mineral (RRUFF ID R060390); this discrepancy is again attributed to the presence of Sb in the reference spectrum. The characteristic ν_1 bands, resulting from As-S and Sb-S stretching vibrations, shift to higher wavenumbers with increasing arsenic composition between 320 and 340 cm^{-1}, with peak positions in close agreement with the FAM-LUZ alloy NP series.[30] In each spectrum, there is a fixed vibrational mode near 494 cm^{-1} that is not present in the Raman spectra of the reference minerals; this stretch is likely due to elemental sulfur (S-S modes) that has reacted with the OLA ligands remaining in the film.[49–51]

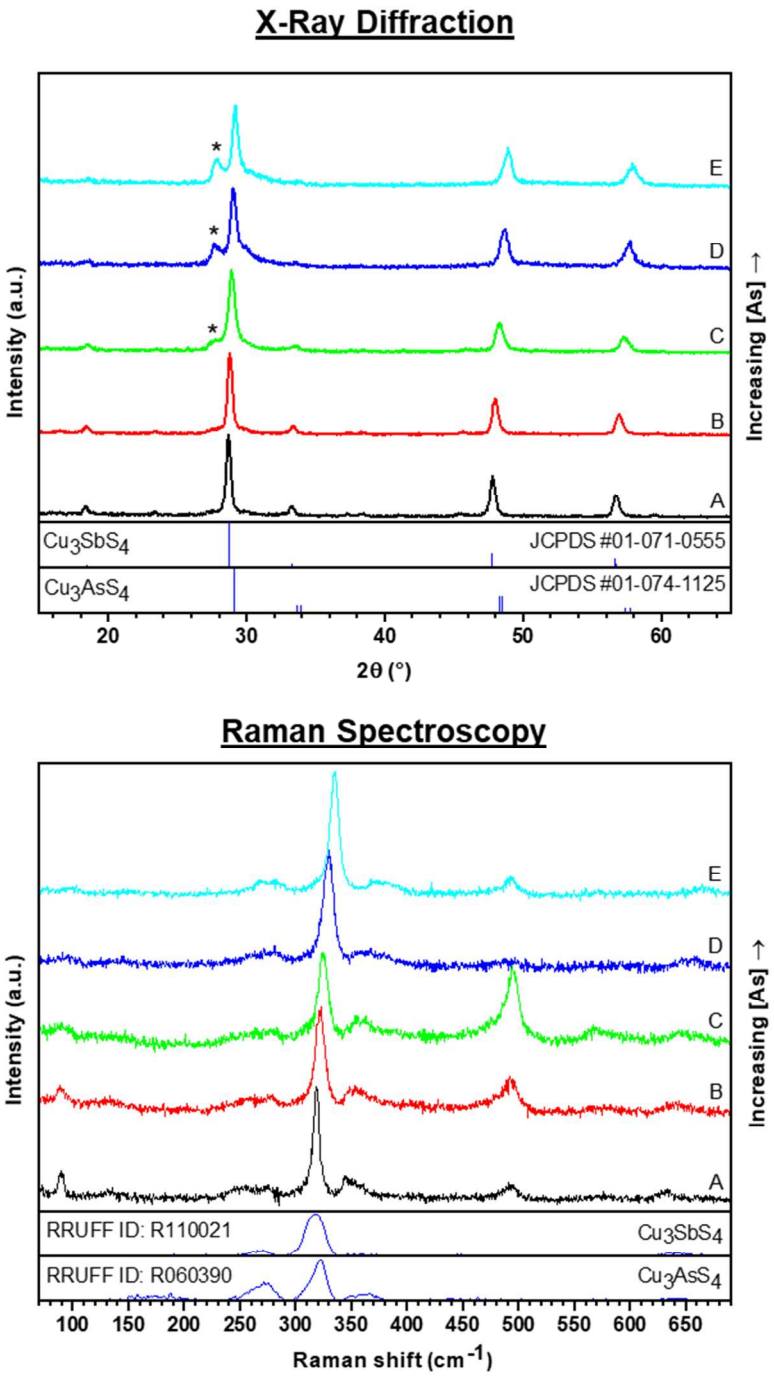

Figure 2. GIXRD and Raman spectra of NPs treated in a sulfur vapor atmosphere at 450 °C for 1 h. (A) $Cu_{12}Sb_4S_{13}$, (B) $Cu_{12}(As_{0.25}Sb_{0.75})_4S_{13}$, (C) $Cu_{12}(As_{0.50}Sb_{0.50})_4S_{13}$, (D) $Cu_{12}(As_{0.75}Sb_{0.25})_4S_{13}$, and (E) $Cu_{12}As_4S_{13}$. GIXRD peaks marked with a * correspond to the (210) plane in orthorhombic enargite Cu_3AsS_4 (JCPDS 01-082-1464).

SEM-EDS measurements (Table 2) were taken to determine bulk compositions of the films after the sulfur heat treatments. The Cu/(Sb+As) ratios are expected to remain identical for stoichiometric TET-TEN and FAM-LUZ compositions. However, after sulfurization, the Cu/(Sb+As) atomic ratios increased relative to the starting NP compositions, indicating a slight loss of pnictogen species. The Sb/(Sb+As) ratios of the mixed-composition samples also increased compared to their starting values, suggesting that arsenic is more readily lost from the films than antimony. Furthermore, Sb was observed in the treated TEN endmember and vice versa, implying that pnictogen species were carried between samples through the vapor phase, as all samples were heated together. Similar phase conversions were observed for NPs heat treated at 350 °C (ESI†, Figure S3).

Table 2. SEM-EDS calculated elemental ratios of $Cu_{12}(As_{1-x}Sb_x)_4S_{13}$ nanoparticles treated in a sulfur atmosphere at 450 °C for 1 h. The standard deviations are based on three measurements from random areas of the samples.

Starting Composition	$\frac{Cu}{Sb+As}$	$\frac{Sb}{Sb+As}$	$\frac{Cu+Sb+As}{S}$
$Cu_{12}Sb_4S_{13}$	3.06 ± 0.05	0.95 ± 0.01	0.99 ± 0.01
$Cu_{12}(As_{0.25}Sb_{0.75})_4S_{13}$	3.33 ± 0.03	0.80 ± 0.01	1.03 ± 0.05
$Cu_{12}(As_{0.50}Sb_{0.50})_4S_{13}$	3.41 ± 0.12	0.66 ± 0.01	1.06 ± 0.04
$Cu_{12}(As_{0.75}Sb_{0.25})_4S_{13}$	3.51 ± 0.05	0.46 ± 0.03	1.02 ± 0.06
$Cu_{12}As_4S_{13}$	3.24 ± 0.02	0.16 ± 0.03	1.08 ± 0.01

Characterization of Nanoparticles Annealed in H_2S

GIXRD data (Fig. 3) obtained for the TET-TEN NP films heat treated in H_2S at 450 °C for 1 h show maintenance of the cubic TET-TEN crystal structure in the mixed As and Sb compositions. These results differ from those of the elemental sulfur treatments, as the phases that exist after H_2S anneals contain As or Sb in the nominal +3 state, rather than +5. In contrast to the stabilized alloy compositions, the endmember NP films underwent phase changes and decomposition at 450 °C. The heat treated $Cu_{12}Sb_4S_{13}$ NP film displays crystallographic planes characteristic of the monoclinic skinnerite phase (SKI, Cu_3SbS_3, JCPDS 01-083-0563), as well as a smaller diffraction peak at 29.8° 2θ that is assignable to TET. Note that SKI is not observed in the sample annealed at 350 °C (ESI†, Figure S4), consistent with previous studies in which SKI was only formed at higher temperatures.[44,52] Additionally, the heat treated $Cu_{12}As_4S_{13}$ film predominately contains digenite $Cu_{1.8}S$ (JCPDS 01-088-2045) impurity peaks. Rietveld refinement (ESI†, Table S2) was used to quantify the phases present after annealing; the data confirm that the endmember films decompose most readily during the H_2S heat treatment. These observations are supported by a previous report suggesting that TEN is unstable at elevated temperature and decomposes into copper sulfide and arsenic sulfide intermediates.[53] However, this decomposition does not occur at 350 °C (ESI†, Figures S4 and S5).

The obtained Raman spectra (Fig. 3) corroborate the stabilization of the TET-TEN cubic crystal structure in the mixed alloy compositions, with peak positions matching those of the starting NP alloys. The treated $Cu_{12}As_4S_{13}$ film also displays peaks characteristic of the TEN phase, though digenite $Cu_{1.8}S$ was not detected in the Raman spectra. These data suggest the formation of localized copper sulfide impurities that are difficult to detect due to the relatively small sampling area. Raman spectra taken on the $Cu_{12}Sb_4S_{13}$ film suggest a multiphase material. The modes near 130 cm^{-1} and 309 cm^{-1} have been reported in SKI thin films,[54] and the mode at

333 cm^{-1} matches closely with the Raman mode of chalcostibite $CuSbS_2$.[55] The presence of multiple phases in the treated film is unsurprising, as TET decomposes to SKI through a $CuSbS_2$ intermediate phase.[56] Note that the Raman spectra of treated $Cu_{12}Sb_4S_{13}$ varied across the surface with some spectra closely matching TET references (ESI†, Figure S6), suggesting inhomogeneous surface composition after heat treatment. In the mixed pnictogen films, the TEN v_1 vibrational mode (near 390 cm^{-1}) was significantly reduced in intensity relative to the TET v_1 vibrational mode (near 350 cm^{-1}), implying more significant losses in As-rich compositions during the H_2S heat treatments.[42] To quantify the losses, SEM-EDS data (Table 3) were acquired on the treated films. The Cu/(Sb+As) ratios increased above the starting values, significantly more than the NPs that were heat treated in elemental sulfur vapors. There was also As present in the Sb endmember (and vice versa), again suggesting the mobility of Sb and As species in the vapor phase. The magnitude of these elemental losses suggests that H_2S is less effective at suppressing decomposition than elemental sulfur.

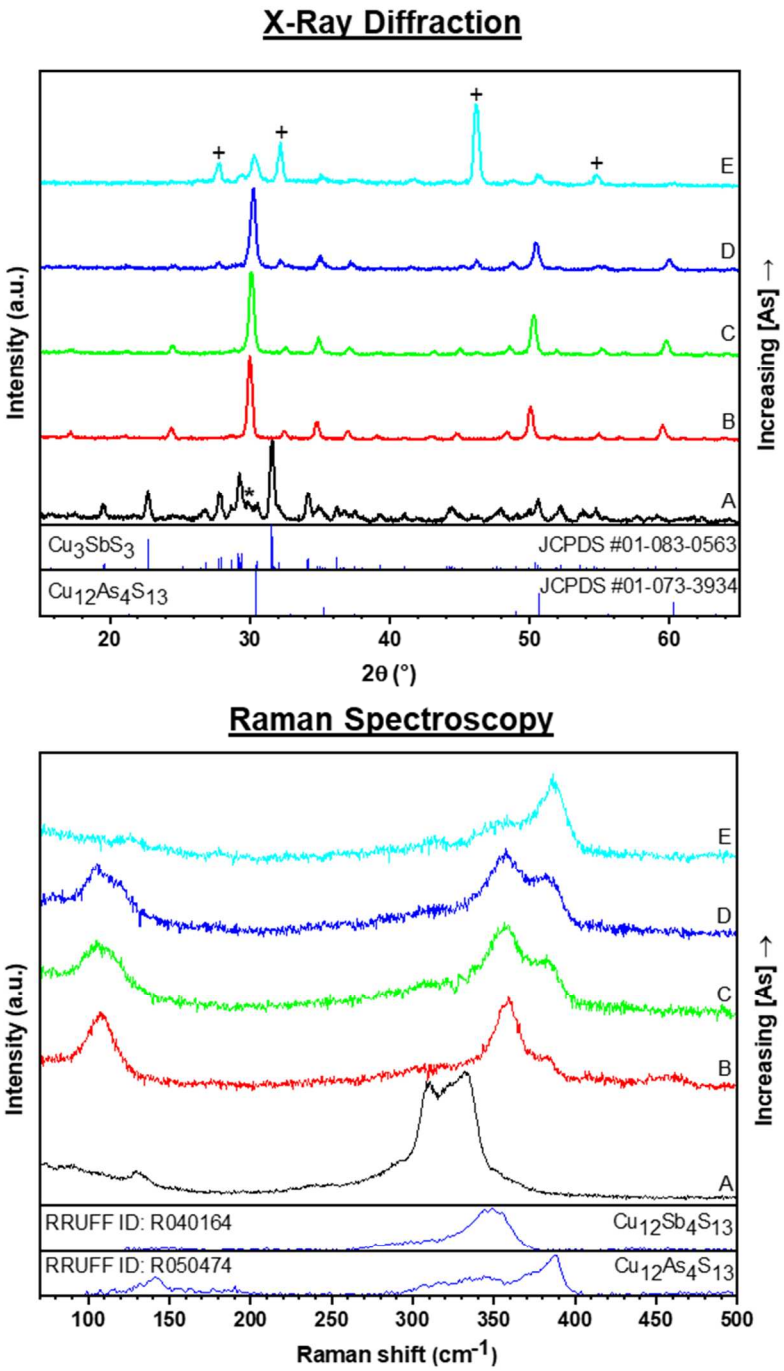

Figure 3. GIXRD and Raman spectra of nanoparticles heated in an H_2S atmosphere at 450 °C for 1 h. (A) $Cu_{12}Sb_4S_{13}$, (B) $Cu_{12}(As_{0.25}Sb_{0.75})_4S_{13}$, (C) $Cu_{12}(As_{0.50}Sb_{0.50})_4S_{13}$, (D) $Cu_{12}(As_{0.75}Sb_{0.25})_4S_{13}$, and (E) $Cu_{12}As_4S_{13}$. The peak marked with (*) in GIXRD spectrum A is attributable to the (222) stretch of tetrahedrite $Cu_{12}Sb_4S_{13}$ (JCPDS 42-560), and the peaks

marked with (+) in spectrum E are attributable to digenite $Cu_{1.8}S$ (JCPDS 01-088-2045). The stretches in Raman spectrum A match with Cu_3SbS_3 and $CuSbS_2$ spectra reported in the literature.[54,55]

Table 3. SEM-EDS calculated elemental ratios of $Cu_{12}(As_{1-x}Sb_x)_4S_{13}$ nanoparticles treated in an H_2S atmosphere at 450 °C for 1 h. The standard deviations are based on three measurements from random areas of the samples.

Starting Composition	$\frac{Cu}{Sb+As}$	$\frac{Sb}{Sb+As}$	$\frac{Cu+Sb+As}{S}$
$Cu_{12}Sb_4S_{13}$	3.64 ± 0.05	0.95 ± 0.01	1.78 ± 0.04
$Cu_{12}(As_{0.25}Sb_{0.75})_4S_{13}$	4.22 ± 0.17	0.83 ± 0.01	1.67 ± 0.08
$Cu_{12}(As_{0.50}Sb_{0.50})_4S_{13}$	4.33 ± 0.64	0.66 ± 0.02	1.60 ± 0.12
$Cu_{12}(As_{0.75}Sb_{0.25})_4S_{13}$	5.40 ± 0.56	0.52 ± 0.02	1.56 ± 0.07
$Cu_{12}As_4S_{13}$	5.33 ± 1.72	0.07 ± 0.05	1.64 ± 0.25

Characterization of Nanoparticles Annealed in Nitrogen

GIXRD (Fig. 4) data show a cubic crystal structure for all TET-TEN compositions, with some Sb-endmember decomposition into skinnerite Cu_3SbS_3 (JCPDS 01-083-0563) and As-endmember decomposition into digenite $Cu_{1.8}S$ (JCPDS 01-088-2045), after heating in nitrogen. Rietveld refinement (ESI†, Table S3) of the GIXRD spectra confirms the relative stability of the mixed alloy compositions when compared with the endmembers. Similar to the H_2S treatments, the Raman spectra (Fig. 4) display peak shifts consistent with the cubic alloy phases, and the magnitude of the TEN v_1 modes are significantly reduced relative to the TET v_1 modes, suggesting more extensive decomposition in As-rich films. SEM-EDS measurements (Table 3) also show a greater loss of arsenic compared to antimony, with Sb/(Sb+As) ratios significantly higher than the starting NP values. The elemental analysis also reveals pnictogen losses in excess

of the maximum observed stable composition ratio of Cu/(Sb+As) = ~3.5:1.[28,44] With the severe losses of arsenic and antimony, it is likely that highly localized copper sulfide species are scattered throughout the film but are undetectable by XRD or Raman. Significant compositional variations were observed across the film's surface, as evidenced by the high standard deviations of the SEM-EDS elemental ratios. It is evident that a nitrogen atmosphere is even less effective at suppressing elemental losses than sulfur and H_2S atmospheres. Note that the cubic crystal structure was unchanged at 350 °C (ESI†, Figure S7).

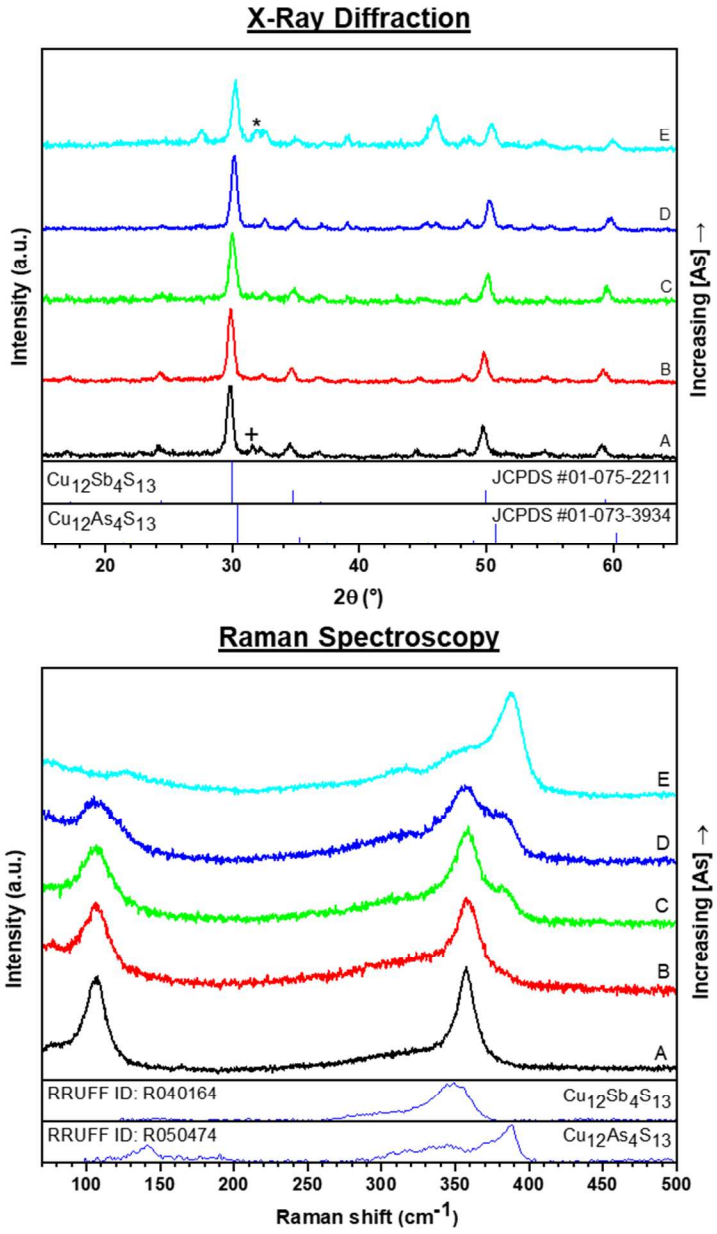

Figure 4. GIXRD and Raman spectra of nanoparticles treated in a nitrogen atmosphere at 450 °C for 1 h. (A) $Cu_{12}Sb_4S_{13}$, (B) $Cu_{12}(As_{0.25}Sb_{0.75})_4S_{13}$, (C) $Cu_{12}(As_{0.50}Sb_{0.50})_4S_{13}$, (D) $Cu_{12}(As_{0.75}Sb_{0.25})_4S_{13}$, and (E) $Cu_{12}As_4S_{13}$. The (+) in GIXRD spectrum (A) denotes a skinnerite Cu_3SbS_3 (JCPDS 01-083-0563) impurity phase, and the (*) in GIXRD spectrum (E) denotes a digenite $Cu_{1.8}S$ impurity phase (JCPDS-01-088-2045).

Table 4. SEM-EDS calculated elemental ratios of $Cu_{12}(As_{1-x}Sb_x)_4S_{13}$ nanoparticles heat treated in a nitrogen atmosphere at 450 °C for 1 h. The standard deviations are based on three measurements from random areas of the samples.

Starting Composition	$\frac{Cu}{Sb+As}$	$\frac{Sb}{Sb+As}$	$\frac{Cu+Sb+As}{S}$
$Cu_{12}Sb_4S_{13}$	3.56 ± 0.07	0.98 ± 0.00	1.40 ± 0.01
$Cu_{12}(As_{0.25}Sb_{0.75})_4S_{13}$	7.08 ± 3.63	0.92 ± 0.09	1.51 ± 0.13
$Cu_{12}(As_{0.50}Sb_{0.50})_4S_{13}$	5.27 ± 0.15	0.81 ± 0.02	1.62 ± 0.07
$Cu_{12}(As_{0.75}Sb_{0.25})_4S_{13}$	9.71 ± 1.81	0.64 ± 0.00	1.72 ± 0.22
$Cu_{12}As_4S_{13}$	11.5 ± 2.8	0.00 ± 0.00	1.71 ± 0.02

In all three atmospheres (Figures S8-S10), grain growth was observed, indicating that the heat treatment protocols may be fine-tuned to produce thin films with uniformly dense grains.

Discussion

The nature of the heat treatment atmosphere was critical for controlling the final phase of the TET-TEN NP alloys. It has been shown that Sb and As exist exclusively in the +5 state in the FAM-LUZ system and mostly in the +3 state in TET-TEN.[22,35,57] Under an elemental sulfur atmosphere, the cubic NPs converted to a tetragonal phase upon annealing at 450 °C. This may be achieved by the simultaneous oxidation of Sb and As (from +3 to +5) and reduction of sulfur (from 0 to -2), forming Cu_3SbS_4-Cu_3AsS_4 alloy phases as described below:

$$Cu_{12}(As_{1-x}Sb_x)_4S_{13} + 3S \rightarrow 4Cu_3As_{1-x}Sb_xS_4$$

Annealing the TET-TEN NPs in 1% H_2S still provides a sulfur-rich atmosphere, but it is slightly reducing instead of oxidizing. Consequently, the Sb and As cations remain in the nominal +3 state rather than the more oxidized +5 state. Additionally, the copper in the digenite $Cu_{1.8}S$ impurity phases primarily exists in the +1 state instead of +2, highlighting the role of H_2S in controlling the nominal oxidation state of the multivalent atoms. The net effect of the H_2S

treatments was to form larger grains of the TET-TEN phases, as evidenced by SEM micrographs (ESI†, Figure S8). These outcomes are not surprising, as H_2S has been used to promote grain growth in other semiconductor systems, albeit in higher concentrations than used here.[58,59]

The loss of Sb and As species from the films is a critical observation with far-reaching implications. As seen in Table 5, pnictogen losses were greatest under a nitrogen atmosphere, followed by H_2S, and finally sulfur vapor. Additionally, As-rich alloys demonstrated greater elemental losses after heat treatment. The SEM-EDS elemental ratios show losses in both the H_2S and nitrogen-treated films, but the GIXRD-calculated ratios suggest less loss. Because the GIXRD data can only provide information regarding the crystalline portion of a material, it is likely that amorphous Cu-S phases exist throughout the treated films. Previous reports on the decomposition mechanisms of TET-TEN and related systems note such elemental sulfur and pnictogen sulfide losses during decomposition, as well as the formation of copper sulfides.[21,53,60–63] It is therefore plausible that the TET-TEN alloy films decompose into binary sulfides and elemental sulfur upon heating. The decomposition phases such as As_2S_3/Sb_2S_3 and sulfur have relatively high vapor pressures and are likely removed during heat treatment in the effluent gas stream. Copper sulfide phases remain and may form crystallites (and hence become detectable by GIXRD) or become trapped at grain boundaries in the final films. It is also important to note that the lattice parameters of the heat treated films also shift linearly as expected from Vegard's law (ESI†, Figure S11), suggesting that the compositions of crystalline grains remain relatively unchanged when compared with the pre-heat treated films.

Table 5. Cu/(Sb+As) ratios for the various 450 °C heat treatments. SEM-EDS data is reproduced from Tables 1-4, and the XRD-calculated results are computed using weight fractions estimated

by Rietveld refinement (ESI†, Tables S2 and S3). GIXRD-calculated results were not determined for the starting NPs or sulfur due to the lack of binary phases appearing in the GIXRD spectra.

Nominal Composition	NPs (EDS)	Sulfur (EDS)	H_2S (EDS)	H_2S (XRD)	N_2 (EDS)	N_2 (XRD)
$Cu_{12}Sb_4S_{13}$	2.86	3.06	3.64	3.01	3.56	3.13
$Cu_{12}(As_{0.25}Sb_{0.75})_4S_{13}$	3.09	3.33	4.22	3.14	7.08	3.14
$Cu_{12}(As_{0.50}Sb_{0.50})_4S_{13}$	3.28	3.41	4.33	3.17	5.27	3.15
$Cu_{12}(As_{0.75}Sb_{0.25})_4S_{13}$	3.45	3.51	5.40	3.68	9.71	3.43
$Cu_{12}As_4S_{13}$	3.10	3.24	5.33	15.10	11.5	7.91

One possible solution to mitigate elemental losses at higher temperatures is to supply an atmosphere containing a partial pressure of pnictogen and sulfur species. Selection of the appropriate atmosphere must be done carefully, as the nominal oxidation state of sulfur in the annealing atmosphere can modify the final phase of the material. Implementation of a closed annealing system[51] or maintaining a vapor pressure of volatile pnictogen sulfide species above the samples[64] are two methods that have been utilized in closely related material systems (Cu_3AsS_4 and $CuSbS_2$, respectively) and may be applied to the TET-TEN family.

The interconversion between cubic TET-TEN NPs and tetragonal FAM-LUZ NPs appears to be reversible if an appropriate annealing atmosphere is used. The FAM-LUZ NP alloy series was synthesized according to a previous report[30] and then heat treated in sulfur, H_2S, and nitrogen atmospheres as described in this manuscript. Under the elemental sulfur atmosphere, the FAM-LUZ phases were maintained, while H_2S and nitrogen anneals resulted in conversion to the TET-TEN phases (ESI†, Figures S12-S14). These two material systems have the same nominal copper-to-pnictogen ratio, suggesting that oxidation or reduction of the cations and the addition or removal of sulfur would result in interconversion between these crystallographic phases.[30] This may be achieved through the use of reducing H_2S (if TET-TEN is desired) or oxidizing

sulfur (if FAM-LUZ is desired) atmospheres during heat treatment; however, controlling pnictogen losses in this setup remains a challenge. Introducing a gas stream of elemental As or Sb in conjunction with H_2S may be an additional route to control these elemental losses. Our results demonstrate the feasibility of stabilizing and/or interconverting the TET-TEN and FAM-LUZ material families by rational selection of an annealing atmosphere, allowing for fabrication of materials with desired crystal structures and optoelectronic properties. Similar chalcogenide NP systems may also display similar behavior, offering new insight and methodologies for synthesis of novel materials.

4. Conclusions

We have reported the first synthesis of $Cu_{12}(As_{1-x}Sb_x)_4S_{13}$ NPs alloys via a two-step hot-injection. NP-based thin films were heat treated in oxidizing (sulfur), reducing (H_2S), and inert (nitrogen) environments to control the phase and composition of the synthesized $Cu_{12}(As_{1-x}Sb_x)_4S_{13}$ NP alloys. Heat treating under an elemental sulfur atmosphere oxidized the antimony and arsenic in the $Cu_{12}(As_{1-x}Sb_x)_4S_{13}$ materials, converting the cubic crystal structure to tetragonal $Cu_3As_{1-x}Sb_xS_4$. Conversely, the oxidation states of antimony and arsenic were maintained when heat treating in H_2S. Additionally, an increase in grain size was observed after all heat treatments. Elemental losses were observed when heating the $Cu_{12}(As_{1-x}Sb_x)_4S_{13}$ films in sulfur, H_2S, and nitrogen, likely due to volatilization of sulfur and binary pnictogen sulfide species. These data provide insight into the stability of this material system and reveal the importance of the heat treatment atmosphere in both stabilizing and controllably converting between the TET-TEN and FAM-LUZ crystal systems. These results provide a foundation for future development of arsenic and antimony chalcogenide-based materials and offer insight into

heat treatment conditions necessary for tuning and optimizing the optoelectronic properties for future device applications.

5. Acknowledgements

This work was supported by the National Science Foundation under grant #1534691-DMR (DMREF: Rapid Design of Earth Abundant Inorganic Materials for Future PVs). The authors would like to acknowledge Joseph Andler for assisting with the table of contents graphic design.

The authors declare no competing financial interests.

Statement of Data Access

The data associated with this manuscript can be found at the project's website: https://datacenterhub.org/groups/dmref1534691

References

1 D. V. Talapin, J.-S. Lee, M. V. Kovalenko and E. V. Shevchenko, *Chem. Rev.*, 2010, **110**, 389–458.

2 P. Reiss, M. Carrière, C. Lincheneau, L. Vaure and S. Tamang, *Chem. Rev.*, 2016, **116**, 10731–10819.

3 C. Coughlan, M. Ibáñez, O. Dobrozhan, A. Singh, A. Cabot and K. M. Ryan, *Chem. Rev.*, 2017, **117**, 5865–6109.

4 M. G. Panthani, J. M. Kurley, R. W. Crisp, T. C. Dietz, T. Ezzyat, J. M. Luther and D. V. Talapin, *Nano Lett.*, 2014, **14**, 670–675.

5 R. W. Crisp, M. G. Panthani, W. L. Rance, J. N. Duenow, P. A. Parilla, R. Callahan, M. S. Dabney, J. J. Berry, D. V. Talapin and J. M. Luther, *ACS Nano*, 2014, **8**, 9063–9072.

6 S. M. McLeod, C. J. Hages, N. J. Carter and R. Agrawal, *Prog. Photovoltaics Res. Appl.*, 2015, **23**, 1550–1556.

7 M. Scheele, N. Oeschler, K. Meier, A. Kornowski, C. Klinke and H. Weller, *Adv. Funct. Mater.*, 2009, **19**, 3476–3483.

8 B. Ananthoju, J. Mohapatra, M. K. Jangid, D. Bahadur, N. V. Medhekar and M. Aslam, *Sci. Rep.*, 2016, **6**, 35369.

9 M. R. Golobostanfard and H. Abdizadeh, *RSC Adv.*, 2016, **6**, 11903–11910.

10 Q. Guo, S. J. Kim, M. Kar, W. N. Shafarman, R. W. Birkmire, E. A. Stach, R. Agrawal and H. W. Hillhouse, *Nano Lett.*, 2008, **8**, 2982–2987.

11 Q. Guo, G. M. Ford, H. W. Hillhouse and R. Agrawal, *Nano Lett.*, 2009, **9**, 3060–3065.

12 W. Wu, Y. Cao, J. V Caspar, Q. Guo, L. K. Johnson, I. Malajovich, H. D. Rosenfeld and K. R. Choudhury, *J. Mater. Chem. C*, 2014, **2**, 3777.

13 C. K. Miskin, W.-C. Yang, C. J. Hages, N. J. Carter, C. S. Joglekar, E. A. Stach and R. Agrawal, *Prog. Photovoltaics Res. Appl.*, 2015, **23**, 654–659.

14 T. R. Martin, J. K. Katahara, C. N. Bucherl, B. W. Krueger, H. W. Hillhouse and C. K. Luscombe, *Chem. Mater.*, 2016, **28**, 135–145.

15 C. J. Hages, M. J. Koeper, C. K. Miskin, K. W. Brew and R. Agrawal, *Chem. Mater.*, 2016, **28**, 7703–7714.

16 C. Wadia, a. P. Alivisatos and D. M. Kammen, *Environ. Sci. Technol.*, 2009, **43**, 2072–2077.

17 X. Lu, D. T. Morelli, Y. Xia, F. Zhou, V. Ozolins, H. Chi, X. Zhou and C. Uher, *Adv.*

Energy Mater., 2013, **3**, 342–348.

18 X. Lu and D. T. Morelli, *Phys. Chem. Chem. Phys.*, 2013, **15**, 5762.

19 K. Suekuni, K. Tsuruta, M. Kunii, H. Nishiate, E. Nishibori, S. Maki, M. Ohta, A. Yamamoto and M. Koyano, *J. Appl. Phys.*, 2013, **113**, 043712.

20 X. Lu and D. Morelli, *J. Electron. Mater.*, 2014, **43**, 1983–1987.

21 R. Chetty, A. Bali and R. C. Mallik, *J. Mater. Chem. C*, 2015, **3**, 12364–12378.

22 R. Chetty, A. Bali, M. H. Naik, G. Rogl, P. Rogl, M. Jain, S. Suwas and R. C. Mallik, *Acta Mater.*, 2015, **100**, 266–274.

23 R. Chetty, P. K. D. S., G. Rogl, P. Rogl, E. Bauer, H. Michor, S. Suwas, S. Puchegger, G. Giester and R. C. Mallik, *Phys. Chem. Chem. Phys.*, 2015, **17**, 1716–1727.

24 Y. Bouyrie, C. Candolfi, A. Dauscher, B. Malaman and B. Lenoir, *Chem. Mater.*, 2015, **27**, 8354–8361.

25 S. Harish, D. Sivaprahasam, M. Battabyal and R. Gopalan, *J. Alloys Compd.*, 2016, **667**, 323–328.

26 J. Heo, R. Ravichandran, C. F. Reidy, J. Tate, J. F. Wager and D. A. Keszler, *Adv. Energy Mater.*, 2015, **5**, 1401506.

27 L. Wang, B. Yang, Z. Xia, M. Leng, Y. Zhou, D.-J. Xue, J. Zhong, L. Gao, H. Song and J. Tang, *Sol. Energy Mater. Sol. Cells*, 2016, **144**, 33–39.

28 S. Maske and B. J. Skinner, *Econ. Geol.*, 1971, **66**, 901–918.

29 F. D. Luce, C. L. Tuttle and B. J. Skinner, *Econ. Geol.*, 1977, **72**, 271–289.

30 R. B. Balow, C. K. Miskin, M. M. Abu-Omar and R. Agrawal, *Chem. Mater.*, 2017, **29**, 573–578.

31 T. Shi, W.-J. Yin, M. Al-Jassim and Y. Yan, *Appl. Phys. Lett.*, 2013, **103**, 152105.

32 L. Yu, R. S. Kokenyesi, D. A. Keszler and A. Zunger, *Adv. Energy Mater.*, 2013, **3**, 43–48.

33 G. J. Snyder and E. S. Toberer, *Nat. Mater.*, 2008, **7**, 105–114.

34 R. B. Balow, E. P. Tomlinson, M. M. Abu-Omar, B. W. Boudouris and R. Agrawal, *J. Mater. Chem. A*, 2016, **4**, 2198–2204.

35 J. van Embden, K. Latham, N. W. Duffy and Y. Tachibana, *J. Am. Chem. Soc.*, 2013, **135**, 11562–11571.

36 K. Ramasamy, H. Sims, W. H. Butler and A. Gupta, *Chem. Mater.*, 2014, **26**, 2891–2899.

37 S. Suehiro, K. Horita, M. Yuasa, T. Tanaka, K. Fujita, Y. Ishiwata, K. Shimanoe and T. Kida, *Inorg. Chem.*, 2015, **54**, 7840–7845.

38 K. Chen, J. Zhou, W. Chen, P. Zhou, F. He and Y. Liu, *Part. Part. Syst. Charact.*, 2015, **32**, 999–1005.

39 R. B. Balow, E. J. Sheets, M. M. Abu-Omar and R. Agrawal, *Chem. Mater.*, 2015, **27**, 2290–2293.

40 L. Vegard, *Zeitschrift fur Phys.*, 1921, **5**, 17–26.

41 A. R. Denton and N. W. Ashcroft, *Phys. Rev. A*, 1991, **43**, 3161–3164.

42 S. Kharbish, E. Libowitzky and A. Beran, *Eur. J. Mineral.*, 2007, **19**, 567–574.

43 M. A. Boles, D. Ling, T. Hyeon and D. V. Talapin, *Nat. Mater.*, 2016, **15**, 141–153.

44 B. J. Skinner, F. D. Luce and E. Makovicky, *Econ. Geol.*, 1972, **67**, 924–938.

45 M. L. Johnson and R. Jeanloz, *Am. Mineral.*, 1983, **68**, 220–226.

46 Y. Bouyrie, C. Candolfi, V. Ohorodniichuk, B. Malaman, A. Dauscher, J. Tobola and B. Lenoir, *J. Mater. Chem. C*, 2015, **3**, 10476–10487.

47 P. Vaqueiro, G. Guélou, A. Kaltzoglou, R. I. Smith, T. Barbier, E. Guilmeau and A. V.

Powell, *Chem. Mater.*, 2017, **29**, 4080–4090.

48 M. Posfai and P. R. Buseck, *Am. Mineral.*, 1998, **83**, 373–382.

49 B. Meyer, *Chem. Rev.*, 1976, **76**, 367–388.

50 B. D. Chernomordik, A. E. Béland, D. D. Deng, L. F. Francis and E. S. Aydil, *Chem. Mater.*, 2014, **26**, 3191–3201.

51 S. A. McClary, J. Andler, C. A. Handwerker and R. Agrawal, *J. Mater. Chem. C*, 2017, **5**, 6913–6916.

52 P. Maiello, G. Zoppi, R. W. Miles, N. Pearsall and I. Forbes, *Sol. Energy Mater. Sol. Cells*, 2013, **113**, 186–194.

53 R. Padilla, Y. Fan and I. Wilkomirsky, *Can. Metall. Q.*, 2001, **40**, 335–342.

54 A. Hussain, R. Ahmed, N. Ali, A. Shaari, J.-T. Luo and Y. Q. Fu, *Surf. Coatings Technol.*, 2017, **319**, 294–300.

55 C. L. McCarthy, P. Cottingham, K. Abuyen, E. C. Schueller, S. P. Culver and R. L. Brutchey, *J. Mater. Chem. C*, 2016, **4**, 6230–6233.

56 T. Barbier, P. Lemoine, S. Gascoin, O. I. Lebedev, A. Kaltzoglou, P. Vaqueiro, A. V. Powell, R. I. Smith and E. Guilmeau, *J. Alloys Compd.*, 2015, **634**, 253–262.

57 X. Lu, W. Yao, G. Wang, X. Zhou, D. T. Morelli, Y. Zhang, H. Chi, S. Hui and C. Uher, *J. Mater. Chem. A*, 2016, 17096–17103.

58 W. Septina, S. Ikeda, Y. Iga, T. Harada and M. Matsumura, *Thin Solid Films*, 2014, **550**, 700–704.

59 M. G. Gang, K. V. Gurav, S. W. Shin, C. W. Hong, J. H. Min, M. P. Suryawanshi, S. A. Vanalakar, D. S. Lee and J. H. Kim, *Phys. status solidi c*, 2015, **12**, 713–716.

60 P. Balaz, J. Briancin and L. Turcaniova, *Thermochim. Acta*, 1995, **249**, 375–381.

61 F.-H. Sun, C.-F. Wu, Z. Li, Y. Pan, A. Asfandiyar, J. Dong and J.-F. Li, *RSC Adv.*, 2017, **7**, 18909–18916.

62 P. Lemoine, C. Bourgès, T. Barbier, V. Nassif, S. Cordier and E. Guilmeau, *J. Solid State Chem.*, 2017, **247**, 83–89.

63 G. H. Albuquerque, K.-J. Kim, J. I. Lopez, A. Devaraj, S. Manandhar, Y.-S. Liu, J. Guo, C. Chang and G. S. Herman, *J. Mater. Chem. A*, 2018, **6**, 8682–8692.

64 F. W. de Souza Lucas, A. W. Welch, L. L. Baranowski, P. C. Dippo, H. Hempel, T. Unold, R. Eichberger, B. Blank, U. Rau, L. H. Mascaro and A. Zakutayev, *J. Phys. Chem. C*, 2016, **120**, 18377–18385.

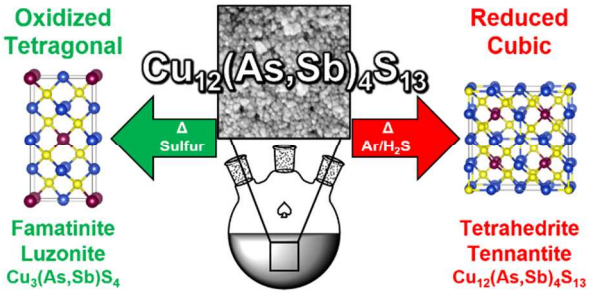

Tetrahedrite-tennantite alloy nanoparticles are synthesized and heat treated under various atmospheres to direct the final phase and composition.